Free-induction-decay ^{4}He magnetometer using a multipass cell

Kaiwen Yi,[1] Yang Liu,[1] Bowen Wang,[1] Wei Xiao,[1] Dong Sheng,[2] Xiang Peng,[1,*] and Hong Guo[1]

[1] *State Key Laboratory of Advanced Optical Communication Systems and Networks, School of Electronics, and Center for Quantum Information Technology, Peking University, Beijing 100871, China*

[2] *Department of Precision Machinery and Precision Instrumentation, Key Laboratory of Precision Scientific Instrumentation of Anhui Higher Education Institutes, University of Science and Technology of China, Hefei 230027, China*

(Received 23 October 2023; revised 3 May 2024; accepted 10 July 2024; published 31 July 2024)

Optically pumped magnetometers (OPMs) based on the free-induction-decay (FID) configuration have recently attracted interest owing to their advantages, such as being calibration-free, easy to operate, and showing reduced light shifts induced by the pump light. Currently, alkali-metal vapor cells have been employed in most of the FID magnetometers. However, the relatively narrow linewidth of the magnetic resonance signal and nonlinear Zeeman (NLZ) effects generate bandwidth limitation and heading errors of these magnetometers in the Earth's field, respectively. In this work, we propose a ^{4}He-based FID magnetometer, which not only has the advantages of being NLZ-free and showing a high bandwidth, but also maintains an enhanced sensitivity assisted by a multipass cell. This magnetometer demonstrates a magnetic field noise floor of 0.34 pT/Hz$^{1/2}$ with a Nyquist-limited bandwidth of 5 kHz, which opens another route for atomic magnetometry using FID signals, and exhibits potential for applications in high-frequency magnetic field detection, such as biomagnetic measurements and magnetic communications in the geomagnetic field.

DOI: 10.1103/PhysRevApplied.22.014084

I. INTRODUCTION

Optically pumped magnetometers (OPMs) have attracted considerable research interest owing to their favorable features, including their capacity for miniaturization [1,2] and the absence of a need for cryogenic cooling [3], while maintaining a comparable sensitivity to superconducting quantum interference devices [4,5]. These make them promising devices for applications in biomagnetic measurements [6–8], fundamental physics [9,10], and space science [11], etc. Currently, the most sensitive atomic magnetometer has been realized with alkali-metal atoms operating in the spin-exchange relaxation-free regime [5], where high atomic density and near-zero ambient magnetic fields are crucial. In comparison, scalar OPMs measure the magnitude of the total magnetic field by monitoring the Larmor precession frequency of atomic spins in the presence of the finite field. The large dynamic range of such OPMs makes them suitable for operation in the Earth's field (10–100 μT), which is beneficial for a wide range of applications, such as geomagnetic mapping [12] and unshielded biomagnetic measurements [13]. Recent progress has led to improvement in the sensitivity of scalar OPMs, including a subfemtotesla OPM implemented using multipass cells in a pump-probe scheme [14], and femtotesla magnetic gradiometers based on intrinsic [15] or synthetic [16] subtraction appropriate for use in Earth-scale fields.

In addition to measurement sensitivity, accuracy and bandwidth are also crucial parameters of scalar OPMs in practical applications, such as searches for permanent electric dipole moment [17–20] where accuracy is the primary requirement, and time-varying biomagnetic measurements that require high bandwidth [13,21]. Traditionally, continuously operated scalar OPMs have been implemented based on the magnetic resonance driven by a radio-frequency field [22,23] or modulated light [24], but these suffer from systematic frequency shifts due to phase errors in the feedback signal [17]. Recently, as alternative configurations for scalar magnetometry, free-induction-decay (FID) magnetometers have aroused intense interest owing to their notable advantages in accuracy [17,25,26]. Since the magnetic field is inferred by directly monitoring the Larmor frequency in the time domain, FID magnetometers are not subject to the aforementioned systematic errors that occur with driven magnetometers and are free of the light shifts generated by the pump light, which is switched off during detection, and thus have greater

*Contact author: xiangpeng@pku.edu.cn

accuracy than continuous-wave pump-probe schemes [25]. These advantages make FID magnetometers among the most sensitive and accurate magnetometers for applications such as unshielded biomagnetic measurements [13], magnetic field imaging [27], and fundamental physics [28]. However, a noteworthy concern is that the alkali-metal vapor cells employed in most of the FID magnetometers reported previously suffer from nonlinear Zeeman (NLZ) effects and the frequency difference between Zeeman transitions in the two hyperfine ground states [29], which generate heading errors especially in the presence of high fields. For instance, the heading errors for ^{87}Rb atoms in the Earth's field reach the level of 15 nT [30].

Besides, the relatively narrow magnetic resonance linewidth may limit the measurement bandwidth of an alkali-metal-based FID magnetometer, which is also constrained by the pump-probe repetition rate. The resulting actual bandwidth is typically of a few hundred Hertz [15,26,27,31]. Although efforts have recently been made to address this issue, (e.g., by increasing spin relaxation rates [26] or pump-probe repetition rates [32]), these approaches improve the bandwidth at the expense of degraded sensitivity. Therefore, an alternative scheme in FID magnetometers with smaller heading errors and higher bandwidth, while maintaining a comparable sensitivity, is becoming necessary and attractive.

Compared with alkali-metal OPMs, ^{4}He OPMs have notable advantages including large dynamic range, high bandwidth, and room-temperature operation without heating [33], though there is a requirement for rf discharge. Combined with these features and recent improvements in sensitivity [34–37], ^{4}He OPMs have become promising alternatives to alkali-metal OPMs in near-zero field detection such as biomagnetic measurements [38]. For scalar measurements, lamp-pumped ^{4}He OPMs have been developed in the last few decades, and widely used in space applications such as Cassini mission [39]. In 1987, McGregor presented a theoretical model that indicated the possibility of a great improvement in sensitivity of ^{4}He OPMs by using a laser to replace the traditional lamp [40]. Later, laser-pumped ^{4}He scalar OPMs have emerged. A typical example is the SWARM ^{4}He magnetometer, which demonstrated an isotropic sensitivity of 1 pT/Hz$^{1/2}$ with a bandwidth up to 300 Hz [41]. Recently, an alternative scheme has been proposed for applications in finite fields by the combined use of a ^{4}He zero-field OPM and closed-loop compensation of the magnetic field [42].

As another attractive scheme in scalar magnetometry, FID magnetometer based on ^{4}He atoms has yet to be explored. Since the metastable ^{4}He atoms do not suffer from NLZ effects and have large spin relaxation rates, an FID magnetometer based on ^{4}He atoms has the potential to present smaller heading errors [43,44] and higher bandwidth than an alkali-metal-based one, which motivates our studies. Benefiting from the technique for developing multipass gas-discharged ^{4}He cell in our previous studies [37], we employ it to improve SNR of the FID signals limited by the relatively low atomic number density of metastable ^{4}He atoms.

In this paper, we propose and demonstrate a high-bandwidth and sensitive FID magnetometer based on metastable ^{4}He atoms. The remainder of the paper is organized as follows. Section II presents the operating principle and experimental scheme of the FID ^{4}He magnetometer. Section III describes the signal-analysis method, parameter optimization, and sensor performance. Finally, the paper is concluded in Sec. IV with a discussion of the characteristics and potential applications of the proposed magnetometer.

II. OPERATING PRINCIPLE AND EXPERIMENTAL SCHEME

The layout of the all-optical FID ^{4}He magnetometer is presented in Fig. 1(a). The static magnetic field $\mathbf{B}_0$ is directed along the z axis, while the orthogonal pump and probe beams are located in the x-y plane, with the pump beam directed along the y axis. The operation of the magnetometer follows two sequential steps, with the timing control pulse sequences shown in Fig. 1(b). The first step is optical pumping with amplitude-modulated circularly polarized light to create spin polarization of metastable ^{4}He atoms. This synchronous optical pumping method has been widely employed in recent studies of FID magnetometers owing to the significant improvement in pumping efficiency that it provides, especially in the presence of high transverse magnetic fields [17,26]. In practice, the modulation scheme can be implemented without prior knowledge of the external field, by scanning the modulation frequency to find the maximum value of the signal amplitude, or utilizing the single-pulse optical pumping to estimate the Larmor frequency before switching to the synchronous optical pumping. In the second step, the pump light is switched off, allowing the atomic spins to freely precess around the external magnetic field. Simultaneously, the Faraday rotation of a weak linearly polarized probe light detuned from D_0 transition ($2\,^3S_1 \rightarrow 2\,^3P_0$) is recorded using balanced polarimetry, enabling magnetic field measurement via extraction of the Larmor frequency by signal-processing techniques described in Sec. III A. As shown in Fig. 1(b), a single measurement cycle of duration T_s consists of a pump stage duration T_p with peak pump power P_p, and a subsequent readout stage duration T_r with constant probe power P_r. According to the Nyquist theorem, the bandwidth of the FID magnetometer is limited to half of the repetition rate $f_d = 1/T_s$.

The dynamics of the spin orientation $\mathbf{S}$ in the FID ^{4}He magnetometer are described by the Bloch equation [17,26]

$$\frac{d\mathbf{S}}{dt} = \gamma \mathbf{S} \times \mathbf{B}_0 - \Gamma_1 S_z \mathbf{e}_z - \Gamma_2 (S_x \mathbf{e}_x + S_y \mathbf{e}_y), \quad (1)$$

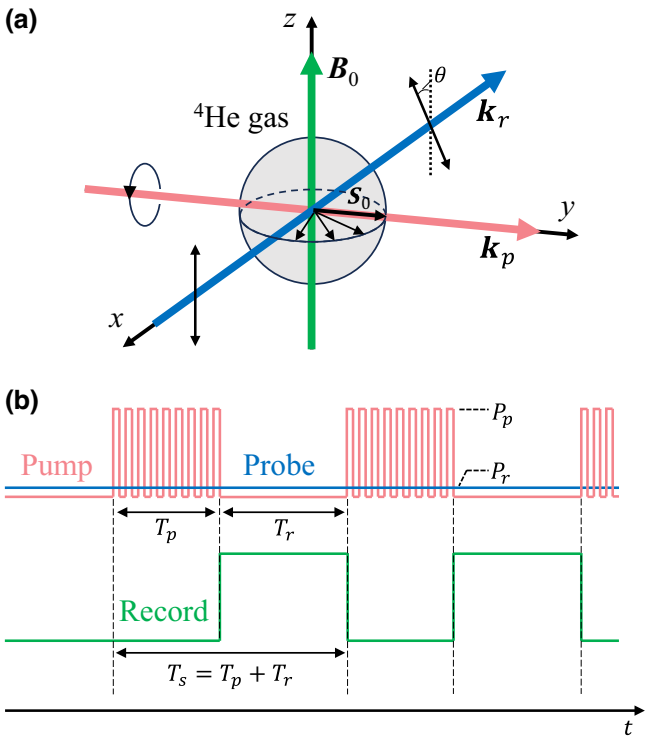

FIG. 1. (a) Geometry of the all-optical FID ^{4}He magnetometer. $\mathbf{B}_0$, the static magnetic field to be measured; $\mathbf{k}_p$ and $\mathbf{k}_r$, light propagation vectors of the circularly polarized pump beam and the linearly polarized probe beam, respectively; $\mathbf{S}_0$, the initial spin orientation created by the pump stage; θ, polarization rotation angle of the probe beam. (b) Timing control pulse sequences of the pump beam, probe beam, and signal recording. In a single measurement cycle of duration $T_s = T_p + T_r$, spin polarization of metastable ^{4}He atoms is created by amplitude-modulated pump light with peak power P_p for a duration T_p, following which the pump light is switched off, and the FID signal read by a weak probe beam with constant power P_r is recorded for a duration T_r.

where $\gamma \simeq 2\pi \times 28.025$ Hz/nT is the gyromagnetic ratio of the ^{4}He atomic metastable state, $\mathbf{B}_0$ is the external magnetic field, and Γ_1 and Γ_2 are the longitudinal and transverse relaxation rates, respectively. We set $\mathbf{B}_0 = B_0\mathbf{e}_z$ and solve Eq. (1) with the initial condition $\mathbf{S}(t=0) = S_0\mathbf{e}_y$, yielding the following solution for the orientation component along the probe beam propagation direction:

$$S_x(t) = S_0 \sin(\omega_L t)\exp(-\Gamma_2 t), \tag{2}$$

where $\omega_L = \gamma B_0$ is the Larmor frequency. The optical rotation angle of the linearly polarized probe beam is proportional to the degree of spin polarization S_x [26], which can be detected by the balanced polarimeter described below.

The experimental setup of the FID ^{4}He magnetometer is shown in Fig. 2. The multipass ^{4}He cell utilized here contains a Herriott cavity, consisting of two cylindrical mirrors with 12.7-mm diameter and 19-mm distance between them. One of the mirrors has a hole of diameter 2.5 mm in its center for entrance and exit of the light beam, which will be reflected 21 times in the cavity with an incident angle of 5°. The cell has external dimensions $15 \times 15 \times 27$ mm^3, and is filled with 74 Pa of ^{4}He gas, which is excited by rf electrodeless discharge to prepare the atoms in the metastable state $2\,^3S_1$. It should be noted that, in contrast to the layer of aluminum oxide (Al_2O_3) used in mirror coatings of multipass alkali-metal cells, we utilize the layers of tantalum pentoxide (Ta_2O_5) and silicon dioxide (SiO_2) to increase the mirror reflectivity, while avoiding impurities generated by collisions between various particles and the coating materials [37].

The pump beam is emitted from a fiber laser at around 1083 nm (NKT Koheras BASIK Y10 with an OEM amplifier) and tuned to the D_0 transition of ^{4}He atoms. The intensity of the pump light is modulated at the Larmor frequency using an acousto-optic modulator (AOM_1, AA Opto-electronic MT110-IR25-3FIO). The modulated laser beam is sent to a fiber-coupled collimator (FCC_1), and its output beam passes through a beam expander to expand the waist diameter to 20 mm ($1/e^2$). The combined use of a half-wave plate (HP_1) and a polarization beam splitter (PBS_1) enables adjustment of the pump light intensity. Then the linear polarization output is transformed into circular polarization using a quarter-wave plate (QP). The peak power of the pump light is 13.5 mW before illuminating the multipass ^{4}He cell. The cell is discharged by an rf source at 38.7 MHz, and located at the center of a seven-layer μ-metal magnetic shield to suppress technical noise contributions. A three-axis Helmholtz coil driven by a stable dc current source (Krohn-Hite Model 523) is used to generate the ambient magnetic field oriented in the z direction.

In the probe light path, another fiber laser is utilized with wavelength set to be red-detuned from the D_0 resonance by 17.6 pm, the probe beam is coupled to FCC_2 and the output beam has a diameter of 1.2 mm. The beam passes through the linear polarizer P_1 and is split into two beams using a partially reflecting mirror (PRM). One of these beams is employed as the probe beam in magnetic field measurements. The other beam is focused and detected by a customized (In, Ga)As photodiode for laser power stabilization through the combined use of a custom-designed proportional-integral-derivative controller (PID) and another acousto-optic modulator (AOM_2). The half-wave plate HP_3 and linear polarizer P_2 are used to adjust the intensity and the axis of linear polarization of the power-stabilized probe beam. The probe beam power is set to be 0.6 mW before entering the gas cell. This beam passes through the hole in the front mirror to enter the cell with an incident angle of 5°, being reflected 21 times between the two mirrors, and then exits from the same

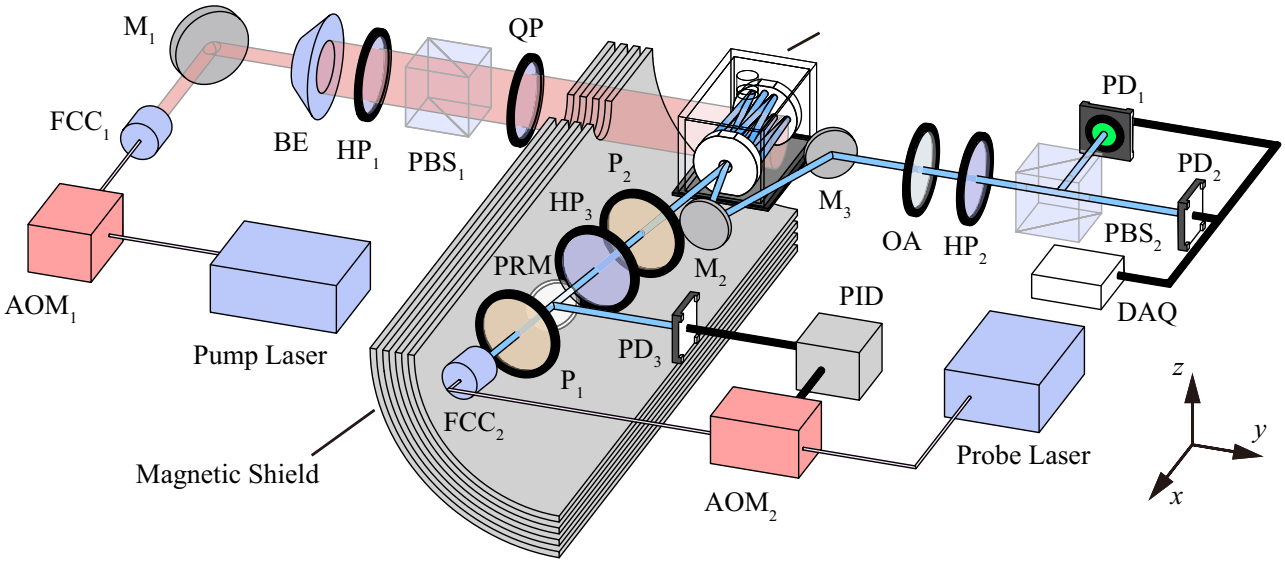

FIG. 2. Schematic of FID ^{4}He magnetometer using a multipass cell. AOM_1, AOM_2, acousto-optic modulators; FCC_1, FCC_2, fiber-coupled collimators; M_1, M_2, M_3, mirrors; BE, beam expander; HP_1, HP_2, HP_3, half-wave plates; PBS_1, PBS_2, polarization beam splitters; QP, quarter-wave plate; OA, optical attenuator; PD_1, PD_2, PD_3, photodiodes; PID, proportional-integral-derivative controller; P_1, P_2, polarizers; PRM, partially reflecting mirror; DAQ, data acquisition.

hole. An optical attenuator (OA) is used to further adjust the intensity of the beam. The rotation of the polarization of the probe beam is measured by a balanced polarimeter oriented at $\pi/4$ relative to the initial polarization. This polarimeter consists of the half-wave plate HP_2, the polarization beam splitter PBS_2, and two customized photodiodes, as shown in Fig. 2. The photocurrent signals from the two channels are processed by a low-noise ac-coupled amplifier (FEMTO Messtechnik DLPCA-200) with a gain of 10^4 V/A, then subtracted and digitized at $f_s = 5$ MHz by a 20-bit acquisition module (NI PXI-5922). The differential signal related to the polarization rotation is given by [45]

$$V_{\text{diff}} = V_{\text{PD}_1} - V_{\text{PD}_2} = V_0 \sin(2\theta), \tag{3}$$

where V_0 is the maximum voltage generated by the full intensity of the probe beam, θ is the polarization rotation angle, which is proportional to the transverse spin polarization, i.e., $S_x(t)$ given by Eq. (2), and can be written as

$$\theta = \theta_0 \sin(\omega_L t) \exp(-\Gamma_2 t). \tag{4}$$

The maximum rotation angle θ_0 is given by [46]

$$\theta_0 = \frac{\pi}{2} n l r_e c S_0 f_{D_0} \,\text{Im}[\mathcal{V}(\nu - \nu_0)], \tag{5}$$

where n is the number density of metastable ^{4}He atoms, l is the optical path length, $r_e = 2.82 \times 10^{-15}$ m is the classical electron radius, and $f_{D_0} = 0.0599$ is the oscillator strength corresponding to the D_0 transition [47]. $\mathcal{V}(\nu - \nu_0)$ represents the Voigt profile in complex form:

$$\mathcal{V}(\nu - \nu_0) = \frac{2\sqrt{\ln 2/\pi}}{\Gamma_G} w\left(\frac{2\sqrt{\ln 2}\,[(\nu - \nu_0) + i\Gamma_L/2]}{\Gamma_G}\right), \tag{6}$$

where $\nu - \nu_0$ is the laser detuning from the D_0 resonance, Γ_L is the linewidth due to the effects of the natural lifetime and pressure broadening, Γ_G is the linewidth due to Doppler broadening, and the complex error function $w(x)$ is given by

$$w(x) = e^{-x^2}[1 - \text{erf}(-ix)]. \tag{7}$$

In our experiment, we observe the noise level of the FID magnetometer in real time by adjusting the probe detuning, and select the value corresponding to the lowest noise level as the optimal detuning. Substitution of Eq. (4) into Eq. (3) gives the FID signal in the general form [14]

$$V_{\text{diff}} = V_0 \sin[2\theta_0 \sin(\omega_L t) \exp(-\Gamma_2 t)]. \tag{8}$$

Since the typical maximum rotation angle θ_0 in this magnetometer is of the order of 100 mrad, the small-angle approximation can be employed to simplify Eq. (8) to

$$V_{\text{diff}} \approx A \sin(\omega_L t) \exp(-\Gamma_2 t), \tag{9}$$

where A is the amplitude of the FID signal.

III. RESULTS AND DISCUSSION

A. Signal analysis and parameter optimization

Various computational approaches have been proposed to extract the Larmor frequency ω_L of the FID signal, such as the least-squares fitting method for the time-domain signal [26,32] or its fast Fourier transform (FFT) spectrum [48,49], and the Hilbert transformation [25,50]. These methods suffer from a general trade-off among their systematic effects, estimation precision, and computational speeds [51], each of which will provide the capability to meet the needs of a specific application. To achieve the real-time signal processing required for the future development of a portable FID ^{4}He magnetometer, an alternative computational approach with high speed and comparable precision is becoming necessary. Thus, we employ here a frequency-domain analysis approach similar to the method reported in Ref. [51], following two steps. In the first step, we calculate the periodogram power spectral density (PSD) of the discretized time-domain signal. In the second step, an algebraic approach is utilized for the rapid extraction of the central frequency of the input signal from its spectrum. We choose 15 points around the peak point in the spectrum and use a weighted average method to find the central frequency

$$f_0 = \frac{\sum_{i=1}^{15} f_i A(f_i)}{\sum_{i=1}^{15} A(f_i)}, \tag{10}$$

where f_i is the frequency value of the ith point and $A(f_i)$ is the corresponding PSD estimate. The use of such an algebraic method ensures that the total time consumption is close to that for the calculation of the PSD, which provides a significant improvement in computational speed while maintaining a sensitivity comparable to that of the least-squares fitting method.

In addition, it should be noted that the selection of the window function in PSD estimations and the points around the peak are useful for both the precision and systematic effects of this approach to frequency estimation, while the former mainly affect the precision and the latter mainly affect the systematic effects [51]. For optimal precision, it is crucial to select an appropriate window function that maximizes the amplitude-to-linewidth ratio of the PSD of the signal. This is due to the fact that a sharper spectral line contains more weights around the central frequency, which is more beneficial for peak finding based on weighted averaging. In our case, we choose Tukey window [52] since it combines the characteristics of rectangular and cosine windows, which can suppress the spectrum leakage while maintaining the central signal shape, thus providing the sharpest spectrum compared with other typical windows. To reduce the systematic effects, a basic principle is that the selected points should cover at least the full width at half maximum of the PSD [51]. This ensures that most of the spectrum information can be used for weighted averaging, making the calculated result more accurate. Besides, the selected points should be symmetrically distributed on both sides of the peak, rather than asymmetrically selected or even selected on one side only, in which cases the calculation results will exhibit obvious biases.

For sensitivity analysis of an FID magnetometer, the Cramér-Rao lower bound (CRLB) is a crucial parameter that determines the lower bound of the statistical uncertainty of extracting the frequency from an FID signal [17]. In the limit of high sampling rate, the CRLB condition for the extraction of the external magnetic field from the angular frequency of a discrete damped sinusoid is given by [17,26]

$$\sigma_{B_0}^2 \geq \frac{24}{\gamma^2 (A/\sigma)^2 N T_r^2} C_2, \tag{11}$$

where A/σ is the SNR, with A the amplitude of the FID signal and σ the standard deviation of the noise, N is the number of data points of the discrete signal, T_r is the readout duration, and C_2 is a correction factor that takes into account the exponential decay of the signal, which can be written as

$$C_2 = \frac{N^3}{12} \frac{(1-z^2)^3(1-z^{2N})}{z^2(1-z^{2N})^2 - N^2 z^{2N}(1-z^2)^2}, \tag{12}$$

where $z = e^{-\Gamma_2/f_s}$, with f_s the sampling rate of the data. Assuming the noise to be white, we can calculate the noise density as

$$\rho_{B_0} = \frac{\sigma_{B_0}}{\sqrt{f_{\mathrm{bw}}}} = \sigma_{B_0}\sqrt{2T_s}, \tag{13}$$

where $f_{\mathrm{bw}} = 1/(2T_s)$ is the measurement bandwidth, with T_s the total time for a single measurement. To maximize the detection bandwidth without sacrificing the measurement sensitivity of the magnetometer, the duration of a single measurement cycle is carefully chosen to be $T_s = 0.1$ ms, with half of the time for optical pumping and half for readout of FID signals. As can be seen in Fig. 4(a), an appreciable spin polarization has been created in such a short duration of $T_p = 50$ μs. This is directly benefited from the relatively short lifetime of the metastable state $2\,^3S_1$ [53,54], which is an advantage of a ^{4}He-based FID magnetometer, since it provides the capability to shorten the pump stage duration T_p while extending the readout stage duration T_r.

In addition, the rf discharge power for the excitation of metastable ^{4}He atoms is also a crucial parameter that affects sensor performance. Figure 3(a) illustrates the dependence of the FID amplitude and the transverse relaxation time on the rf discharge power, experienced in a bias field of 11.4 μT. It is shown that increasing the rf discharge power will improve the SNR of FID signals owing

to the increasing number density of metastable ^{4}He atoms, as indicated by the maximum rotation angle θ_0 in Eq. (5). We note here that such an increase in atomic number density is valid in the low-pressure regime, where the influence of Penning ionization can be neglected [54]. However, increasing the rf power will also degrade the transverse relaxation time T_2, since the collisional processes between the different species in the plasma that destroy the spin coherence become more significant. Thus, according to the CRLB condition in Eq. (11), the trade-off between these two parameters will result in an optimum sensitivity occurring at a specific rf power. As shown in Fig. 3(b), this is confirmed by the trends of variation of the noise floor of the magnetometer and the CRLB condition with rf discharge power, which exhibit good consistency and indicate that the optimum sensitivity occurs at an rf power of 1 W. Hence, we fix this value for the following experiments. In addition, it can be seen that the actual sensitivity performance of the magnetometer is worse than the CRLB limit. This is expected, since the signal-analysis method proposed here sacrifices sensitivity to achieve a significant improvement in speed [51], benefiting for the development of high-bandwidth FID magnetometers. Obviously, an alternative analysis method, such as least-squares fitting, can be employed to closely approach the CRLB limit if a particular application does not require a high signal processing speed.

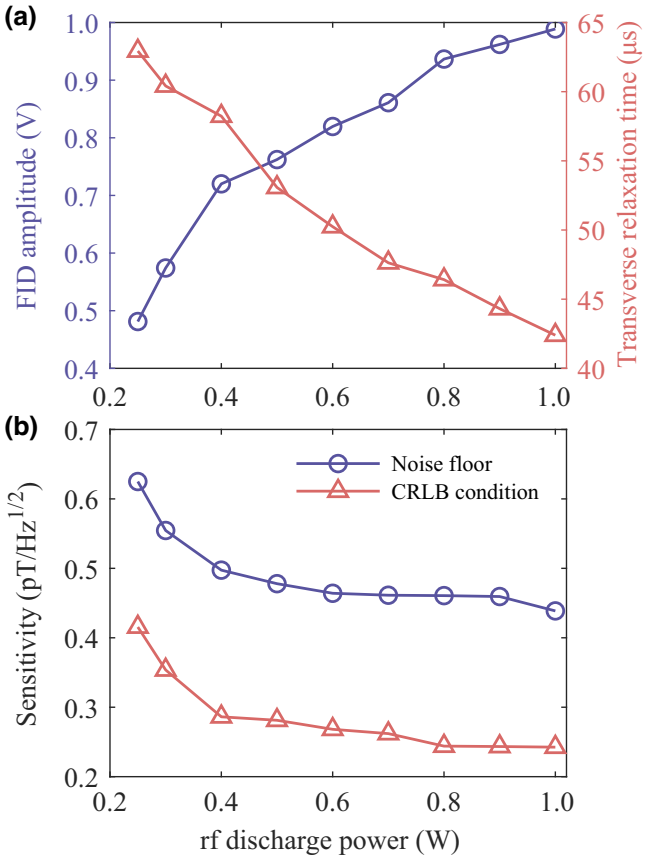

FIG. 3. (a) Dependence of FID amplitude (blue line with circles) and transverse relaxation time (orange line with triangles) on the rf discharge power. (b) Noise floors of the magnetometer (blue line with circles) and the CRLB conditions (orange line with triangles) for different rf discharge powers. In these cases, the bias field is kept at 11.4 μT and the pump-probe repetition rate is kept at 10 kHz.

B. Performance analysis

Figure 4(a) shows a sample of the raw experimental signals with optimized experimental conditions. To demonstrate the significant contribution of the multipass cell in implementing a high-sensitivity ^{4}He-based FID magnetometer, we employ a cylindrical single-pass cell to repeat this experiment for comparison. The single-pass cell has a diameter of 15 mm and a length of 30 mm, and is also filled with 74 Pa of ^{4}He gas. All experimental parameters of the pump and probe light are kept the same for both cases, while the frequency and the power of the rf electrodeless discharge are slightly different due to the different optimized operation conditions. As shown in Fig. 4(b), the amplitude of the FID signal generated by the multipass cell is about 20 times larger than that of the single-pass cell, which is consistent with the reflection times of the probe beam in the multipass cell.

To estimate the sensitivity of the magnetometers, a set of FID signals in 10 s is acquired. Each individual FID signal is processed by the proposed peak finding routine described by Eq. (10) to provide the magnetic field data. We then calculate the noise spectral densities (NSDs) of the 10 s of magnetic field data using Welch's method and smooth the NSD data to finally obtain Fig. 4(c). It can be seen that the noise floor of the FID magnetometer with a multipass cell is 0.44 pT/Hz$^{1/2}$, while that in the case of a single-pass cell is 7.49 pT/Hz$^{1/2}$. The spikes in the NSDs for both cases are caused by power-line interference. Additionally, by fitting the data of the FID signals shown in Fig. 4(b) to the damped sinusoid model described by Eq. (9), the relevant experimental parameters required for CRLB estimation can be extracted. On substitution of all the parameters into Eq. (11), the CRLB condition for the FID signal with multipass cell is estimated to be $\rho_{B_0} \geq 0.24$ pT/Hz$^{1/2}$ for a cycle time of $T_s = 0.1$ ms. Also, the calculation is repeated for the case of single-pass cell, the CRLB condition for which is estimated to be $\rho_{B_0} \geq 3.84$ pT/Hz$^{1/2}$. The relatively poor sensitivity of the FID magnetometer employing a single-pass ^{4}He cell compared with those of alkali-metal cells [17,26,32] is to be expected, since the number density of metastable ^{4}He atoms is of the order of 10^{10}–10^{11} cm^{-3}, which is generally 2 orders of magnitude smaller than that of alkali-metal atoms [14,32,45], resulting in a low SNR as expected from Eq. (5). Therefore, introducing a multipass cell to increase the optical path length l is an effective way to enhance

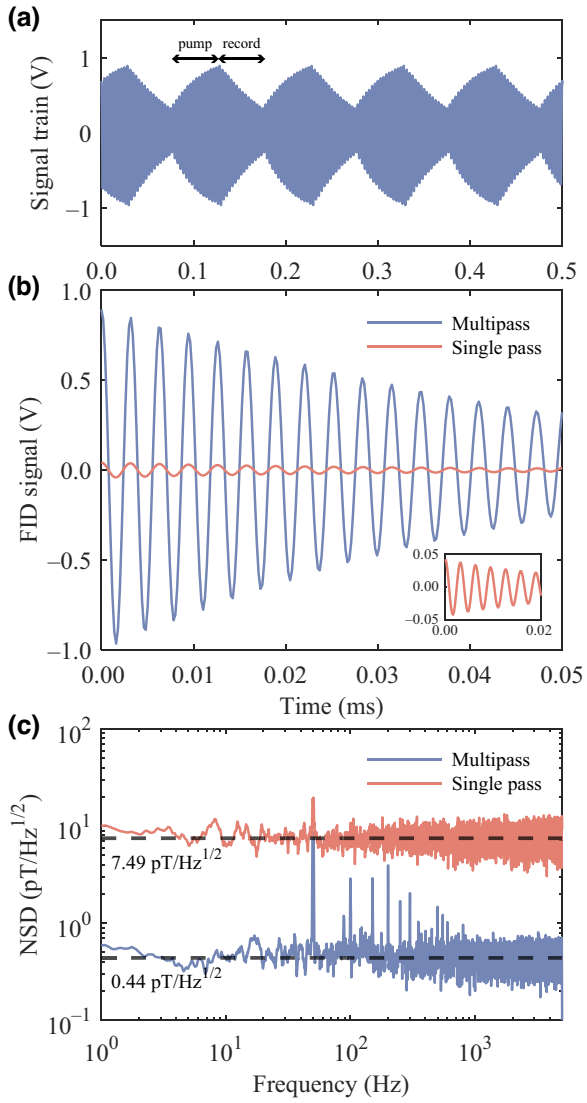

FIG. 4. (a) Sample of signal train acquired by the polarimeter in an ambient field of 11.4 μT. The pump-probe repetition rate is set to 10 kHz. (b) FID signals generated by the multipass ^{4}He cell (blue line) and the single-pass cell with 15-mm diameter and 30-mm length (orange line). (c) Magnetic field noise spectral densities (NSDs) of the FID ^{4}He magnetometer using the multipass cell (blue line) and the single-pass cell (orange line).

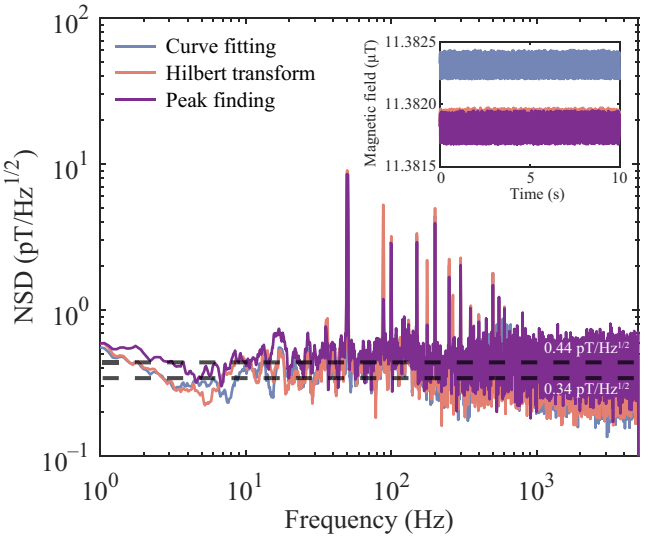

FIG. 5. Measured magnetic fields (inset) and noise spectral densities (NSDs) of the FID ^{4}He magnetometer using the multipass cell based on the least-squares fitting (blue line), the Hilbert transform (orange line), and the peak finding methods (purple line), respectively.

the SNR of FID signal, and thus lift the limitation of low sensitivity of an FID ^{4}He magnetometer.

Finally, we would like to briefly discuss the limitations on the sensitivity of our magnetometer. The precision of the proposed signal analysis method and the magnetic field noise generated by the current source are two main factors responsible for the noise floor of 0.44 pT/Hz$^{1/2}$. As shown in Fig. 5, replacing the peak-finding method with the least-squares fitting or the Hilbert-transform methods yields a noise floor of 0.34 pT/Hz$^{1/2}$, which can be further improved by replacing the current source with one of better performance. In addition, it can be seen from the inset that the magnetic field values obtained by these signal processing methods exhibit a good consistency within 0.5 nT, while the results obtained by the least-squares fitting method show slight differences compared to those obtained by the Hilbert transform and the peak-finding methods. Such differences may arise from the fact that the experimental FID signals deviate slightly from the anticipated damped sinusoid model described by Eq. (9), leading to systematic effects when employing the least-squares fitting method [25].

A significant advantage of ^{4}He-based FID magnetometers is their potential to increase the detection bandwidth while maintaining the same sensitivity, which is directly benefited from the large spin relaxation rate of metastable ^{4}He atoms. To demonstrate the capability of this magnetometer in reconstructing an ac magnetic field signal, we set the bias field B_z to about 5.65 μT, which is modulated by another weak sinusoidal field with peak-to-peak amplitude of about 11 nT oscillating at 2.5 kHz. The repetition rate of the magnetometer is set to be 10 kHz as before, resulting in four data points in one oscillation period of the ac signal. A subset of the measured magnetic field data with a duration of 1.2 ms is shown in Fig. 6(a). Note that a digital bandpass Butterworth filter has been applied to the data to remove the noise component outside the passband, where the lower and upper cutoff frequencies are 2 and 3 kHz, respectively. The values of the magnetic field data can be well fitted by the sinusoidal function

$$B = B_m \sin(2\pi f_m t + \varphi_0) + B_0, \tag{14}$$

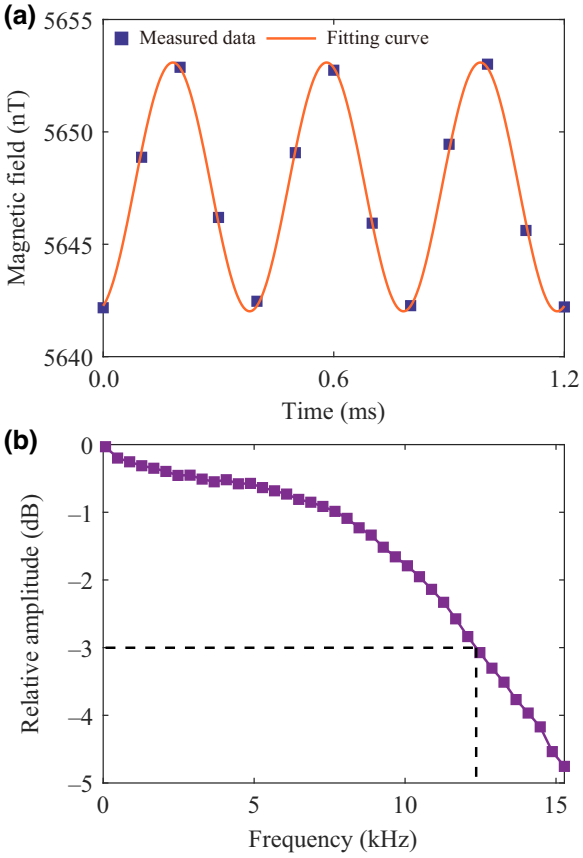

FIG. 6. (a) Subset of ac magnetic field values measured by the magnetometer (blue dots), and the corresponding fitting curve giving a good reconstruction of the sinusoidal waveform oscillating at 2.5 kHz (orange line). (b) Frequency response of the FID ^{4}He magnetometer using a multipass cell. The pump-probe repetition rate is set to 10 kHz, leading to a Nyquist-limited bandwidth of 5 kHz. Data points with frequencies exceeding the Nyquist limit were measured through aliasing. The −3-dB bandwidth is estimated to be 12.36 kHz, as indicated by the dashed lines.

providing fitting results with peak-to-peak amplitude $B_{pp} = 2B_m = 11.1$ nT, modulation frequency $f_m = 2499.58$ Hz, and amplitude of the bias field $B_0 = 5647.6$ nT. The coefficient of determination that measures the goodness of the fit is $R^2 = 0.998$. These results show good agreement with the set experimental parameters, demonstrating the capability of the magnetometer to recover a weak and high-frequency ac magnetic field signal in the presence of a high static bias field.

The frequency response of the FID ^{4}He magnetometer is obtained by a frequency-domain-based method. First, we apply a sinusoidal magnetic field with peak-to-peak amplitude of 114 pT at a certain frequency in a bias field of 11.4 μT. Then we employ the same routine depicted by Fig. 4(c) to obtain the NSD of the magnetometer, and record the amplitude of the spike at the frequency of alternating field. By changing the frequency of the field and calculating relative amplitudes of the spikes at different frequencies, we can finally depict Fig. 6(b). Note that the data points with frequencies beyond the Nyquist limit are measured through aliasing, which folds back the data into a detectable bandwidth. It is shown that the relative amplitude does not decrease significantly within the Nyquist-limited bandwidth of 5 kHz. This benefits directly from the large transverse relaxation rate of metastable ^{4}He atoms, which reaches the order of 20 kHz as indicated in Fig. 3(a). It means that the sensor bandwidth is limited by the pump-probe repetition rate rather than by Γ_2, which indicates that a further increase in the repetition rate provides a way to enhance bandwidth without loss of sensitivity. In addition, the subtle interplay between the repetition rate and transverse relaxation rate results in the estimated −3-dB bandwidth to be 12.36 kHz. A detailed analysis of the interplay and its impact on the frequency response of the sensor can be found in Ref. [31]. However, we would like to emphasize here that the actual effective measurement bandwidth is still limited by the pump-probe repetition rate of the sensor via the Nyquist theorem [32], rather than the −3-dB frequency. Even so, the FID ^{4}He magnetometer achieves the Nyquist-limited bandwidth of 5 kHz, far exceeding the performance of previously reported alkali-metal-based FID magnetometers [17,26,32], while maintaining comparable sensitivity.

IV. CONCLUSIONS AND OUTLOOK

In conclusion, we have proposed and demonstrated an FID ^{4}He magnetometer operated in Earth's field using a multipass cell. An algebraic approach has been developed to extract the Larmor frequency of the FID signals. It provides an improvement in calculation speed compared with traditional methods such as least-squares fitting and the Hilbert transformation, thus facilitating the future development of portable FID ^{4}He magnetometers requiring real-time signal processing, though the possible systematic effects introduced by the fast data-analysis method require more thorough study in future work. Combined with the notable advantages of metastable ^{4}He atoms, including the large spin relaxation rates, the relatively short time required to polarize atoms, and high gyromagnetic ratio of the atomic state, we have presented an attractive scheme for FID magnetometry with high bandwidth and high sensitivity assisted by a multipass cell. The significance of such a cell in the implementation of FID ^{4}He magnetometer has been illustrated, which shows a considerable enhancement of the SNR of FID signals, thus directly improving the sensitivity as expected in CRLB estimation. The experimental results demonstrate a magnetic field noise floor of 0.44 pT/Hz$^{1/2}$ with the Nyquist-limited bandwidth of 5 kHz, whereas the CRLB condition is estimated to be $\rho_{B_0} \geq 0.24$ pT/Hz$^{1/2}$. Replacing the peak-finding method with the least-squares fitting or Hilbert-transform methods yields a noise floor of

0.34 pT/Hz$^{1/2}$, which can be further improved by using a better current source.

Apart from these performance, we would like to briefly discuss the potential heading errors of this sensor. Since the metastable ^{4}He atoms have the advantage of NLZ-free and the sensor is free of the light shifts generated by the pump light, two major sources of heading errors are eliminated. Moreover, as the detuned probe light is linearly polarized, the vector light shifts are largely suppressed. The remaining heading errors are primarily caused by the tensor light shifts induced by the probe light. Consequently, the proposed magnetometer scheme has the potential to exhibit small heading errors, though the experimental verification needs to be conducted in the future work.

Given its advantages, including room-temperature operation and an all-optical setup without crosstalk caused by rf magnetic fields when arrayed, the proposed FID ^{4}He magnetometer has potential for biomagnetic applications such as unshielded magnetocardiogram (MCG) measurement [13] and the detection of animal nerve impulses [21]. Besides, this magnetometer is an attractive quantum sensor for applications in magnetic field communications [55] due to its high bandwidth. Finally, we want to emphasize that the multipass ^{4}He cell used in this magnetometer is also beneficial for the sensitivity improvement of other OPM schemes, such as Bell-Bloom, nonlinear magneto-optical rotation, and parametric resonance. The techniques for developing multipass gas-discharged cells, and increasing the reflection times in the future, open the possibility for nuclear spin squeezing in helium-3 [56].

ACKNOWLEDGMENTS

This work was supported by the National Natural Science Foundation of China (Grant No. 62375002).

[1] P. D. D. Schwindt, S. Knappe, V. Shah, L. Hollberg, J. Kitching, L.-A. Liew, and J. Moreland, Chip-scale atomic magnetometer, Appl. Phys. Lett. **85**, 6409 (2004).

[2] J. Kitching, Chip-scale atomic devices, Appl. Phys. Lett. **5**, 031302 (2018).

[3] D. Budker and M. V. Romalis, Optical magnetometry, Nat. Phys. **3**, 227 (2007).

[4] I. K. Kominis, T. W. Kornack, J. C. Allred, and M. V. Romalis, A subfemtotesla multichannel atomic magnetometer, Nature **422**, 596 (2003).

[5] H. B. Dang, A. C. Maloof, and M. V. Romalis, Ultrahigh sensitivity magnetic field and magnetization measurements with an atomic magnetometer, Appl. Phys. Lett. **97**, 151110 (2010).

[6] E. Boto, N. Holmes, J. Leggett, G. Roberts, V. Shah, S. S. Meyer, L. D. Muñoz, K. J. Mullinger, T. M. Tierney, S. Bestmann, G. R. Barnes, R. Bowtell, and M. J. Brookes, Moving magnetoencephalography towards real-world applications with a wearable system, Nature **555**, 657 (2018).

[7] A. Borna, T. R. Carter, A. P. Colombo, Y.-Y. Jau, J. McKay, M. Weisend, S. Taulu, J. M. Stephen, and P. D. D. Schwindt, Non-invasive functional-brain-imaging with an OPM-based magnetoencephalography system, PLoS ONE **15**, 1 (2020).

[8] K. Kim, S. Begus, H. Xia, S.-K. Lee, V. Jazbinsek, Z. Trontelj, and M. V. Romalis, Multi-channel atomic magnetometer for magnetoencephalography: A configuration study, NeuroImage **89**, 143 (2014).

[9] S. Pustelny, D. F. Kimball, C. Pankow, M. P. Ledbetter, P. Wlodarczyk, P. Wcislo, M. Pospelov, J. R. Smith, J. Read, W. Gawlik, and D. Budker, The Global Network of Optical Magnetometers for Exotic Physics (GNOME): A novel scheme to search for physics beyond the Standard Model, Ann. Phys. **525**, 659 (2013).

[10] C. Abel *et al.*, Measurement of the permanent electric dipole moment of the neutron, Phys. Rev. Lett. **124**, 081803 (2020).

[11] A. Balogh, Planetary magnetic field measurements: Missions and instrumentation, Space Sci. Rev. **152**, 23 (2010).

[12] M. N. Nabighian, V. J. S. Grauch, R. O. Hansen, T. R. LaFehr, Y. Li, J. W. Peirce, J. D. Phillips, and M. E. Ruder, The historical development of the magnetic method in exploration, Geophysics **70**, 33ND (2005).

[13] M. E. Limes, E. L. Foley, T. W. Kornack, S. Caliga, S. McBride, A. Braun, W. Lee, V. G. Lucivero, and M. V. Romalis, Portable magnetometry for detection of biomagnetism in ambient environments, Phys. Rev. Appl. **14**, 011002 (2020).

[14] D. Sheng, S. Li, N. Dural, and M. V. Romalis, Subfemtotesla scalar atomic magnetometry using multipass cells, Phys. Rev. Lett. **110**, 160802 (2013).

[15] V. G. Lucivero, W. Lee, N. Dural, and M. V. Romalis, Femtotesla direct magnetic gradiometer using a single multipass cell, Phys. Rev. Appl. **15**, 014004 (2021).

[16] V. G. Lucivero, W. Lee, M. E. Limes, E. L. Foley, T. W. Kornack, and M. V. Romalis, Femtotesla nearly-quantum-noise-limited pulsed gradiometer at Earth-scale fields, Phys. Rev. Appl. **18**, L021001 (2022).

[17] Z. D. Grujić, P. A. Koss, G. Bison, and A. Weis, A sensitive and accurate atomic magnetometer based on free spin precession, Eur. Phys. J. D **69**, 1 (2015).

[18] I. Altarev *et al.*, Towards a new measurement of the neutron electric dipole moment, Nucl. Instrum. Methods Phys. Res. A **611**, 133 (2009).

[19] S. Groeger, G. Bison, J.-L. Schenker, R. Wynands, and A. Weis, A high-sensitivity laser-pumped M_x magnetometer, Eur. Phys. J. D **38**, 239 (2006).

[20] C. Abel *et al.*, Optically pumped Cs magnetometers enabling a high-sensitivity search for the neutron electric dipole moment, Phys. Rev. A **101**, 053419 (2020).

[21] K. Jensen, B. H. Bentzen, and E. S. Polzik, in *Flexible High Performance Magnetic Field Sensors: On-Scalp Magnetoencephalography and Other Applications*, edited by E. Labyt, T. Sander, and R. Wakai (Springer International Publishing, Cham, 2022), p. 33.

[22] A. Weis, G. Bison, and A. S. Pazgalev, Theory of double resonance magnetometers based on atomic alignment, Phys. Rev. A **74**, 033401 (2006).

[23] A. Weis, G. Bison, and Z. D. Grujić, in *High Sensitivity Magnetometers*, edited by A. Grosz, M. J. Haji-Sheikh, and S. C. Mukhopadhyay (Springer International Publishing, Cham, 2017), p. 361.

[24] Z. D. Grujić and A. Weis, Atomic magnetic resonance induced by amplitude-, frequency-, or polarization-modulated light, Phys. Rev. A **88**, 012508 (2013).

[25] D. Hunter, T. E. Dyer, and E. Riis, Accurate optically pumped magnetometer based on Ramsey-style interrogation, Opt. Lett. **47**, 1230 (2022).

[26] D. Hunter, S. Piccolomo, J. D. Pritchard, N. L. Brockie, T. E. Dyer, and E. Riis, Free-induction-decay magnetometer based on a microfabricated Cs vapor cell, Phys. Rev. Appl. **10**, 014002 (2018).

[27] C. Liu, H. Dong, and J. Sang, Submillimeter-resolution magnetic field imaging with digital micromirror device and atomic vapor cell, Appl. Phys. Lett. **119**, 114002 (2021).

[28] M. Rosner, D. Beck, P. Fierlinger, H. Filter, C. Klau, F. Kuchler, P. Rößner, M. Sturm, D. Wurm, and Z. Sun, A highly drift-stable atomic magnetometer for fundamental physics experiments, Appl. Phys. Lett. **120**, 161102 (2022).

[29] Z. Wang, X. Peng, R. Zhang, H. Luo, J. Li, Z. Xiong, S. Wang, and H. Guo, Single-species atomic comagnetometer based on ^{87}Rb atoms, Phys. Rev. Lett. **124**, 193002 (2020).

[30] W. Lee, V. G. Lucivero, M. V. Romalis, M. E. Limes, E. L. Foley, and T. W. Kornack, Heading errors in all-optical alkali-metal-vapor magnetometers in geomagnetic fields, Phys. Rev. A **103**, 063103 (2021).

[31] D. Hunter, R. Jiménez-Martínez, J. Herbsommer, S. Ramaswamy, W. Li, and E. Riis, Waveform reconstruction with a Cs based free-induction-decay magnetometer, Opt. Express **26**, 30523 (2018).

[32] S. Li, J. Liu, M. Jin, K. T. Akiti, P. Dai, Z. Xu, and T. E.-T. Nwodom, A kilohertz bandwidth and sensitive scalar atomic magnetometer using an optical multipass cell, Measurement **190**, 110704 (2022).

[33] D. Budker and D. F. Kimball, *Optical Magnetometry* (Cambridge University Press, Cambridge, 2013).

[34] F. Beato, E. Belorizky, E. Labyt, M. Le Prado, and A. Palacios-Laloy, Theory of a ^{4}He parametric-resonance magnetometer based on atomic alignment, Phys. Rev. A **98**, 053431 (2018).

[35] E. Labyt, M.-C. Corsi, W. Fourcault, A. Palacios Laloy, F. Bertrand, F. Lenouvel, G. Cauffet, M. Le Prado, F. Berger, and S. Morales, Magnetoencephalography with optically pumped ^{4}He magnetometers at ambient temperature, IEEE Trans. Med. Imaging **38**, 90 (2019).

[36] W. Fourcault, R. Romain, G. Le Gal, F. Bertrand, V. Josselin, M. Le Prado, E. Labyt, and A. Palacios-Laloy, Helium-4 magnetometers for room-temperature biomedical imaging: Toward collective operation and photon-noise limited sensitivity, Opt. Express **29**, 14467 (2021).

[37] Y. Liu, X. Peng, H. Wang, B. Wang, K. Yi, D. Sheng, and H. Guo, Femtotesla ^{4}He magnetometer with a multipass cell, Opt. Lett. **47**, 5252 (2022).

[38] T. P. Gutteling, M. Bonnefond, T. Clausner, S. Daligault, R. Romain, S. Mitryukovskiy, W. Fourcault, V. Josselin, M. Le Prado, A. Palacios-Laloy, E. Labyt, J. Jung, and D. Schwartz, A new generation of OPM for high dynamic and large bandwidth MEG: The ^{4}He OPMs—first applications in healthy volunteers, Sensors **23**, 2801 (2023).

[39] E. J. Smith, M. K. Dougherty, C. T. Russell, and D. J. Southwood, Scalar helium magnetometer observations at Cassini Earth swing-by, J. Geophys. Res. Space Phys. **106**, 30129 (2001).

[40] D. D. McGregor, High-sensitivity helium resonance magnetometers, Rev. Sci. Instrum. **58**, 1067 (1987).

[41] T. Jager, J.-M. Léger, F. Bertrand, I. Fratter, and J.-C. Lalaurie, in *SENSORS, 2010 IEEE* (IEEE, Waikoloa, HI, USA, 2010), p. 2392.

[42] F. Bertrand, T. Jager, A. Boness, W. Fourcault, G. Le Gal, A. Palacios-Laloy, J. Paulet, and J. M. Léger, A ^{4}He vector zero-field optically pumped magnetometer operated in the Earth-field, Rev. Sci. Instrum. **92**, 105005 (2021).

[43] R. Jiménez-Martínez and S. Knappe, in *High Sensitivity Magnetometers*, edited by A. Grosz, M. J. Haji-Sheikh, and S. C. Mukhopadhyay (Springer International Publishing, Cham, 2017), p. 523.

[44] R. E. Slocum, D. D. McGregor, and A. W. Brown, in *Optical Magnetometry*, edited by D. Budker and D. F. Jackson Kimball (Cambridge University Press, Cambridge, 2013), p. 190.

[45] S. Li, P. Vachaspati, D. Sheng, N. Dural, and M. V. Romalis, Optical rotation in excess of 100 rad generated by Rb vapor in a multipass cell, Phys. Rev. A **84**, 061403 (2011).

[46] S. J. Seltzer, *Developments in alkali-metal atomic magnetometry*, Ph.D. thesis, Princeton University, 2008.

[47] W. L. Wiese and J. R. Fuhr, Accurate atomic transition probabilities for hydrogen, helium, and lithium, J. Phys. Chem. Ref. Data **38**, 565 (2009).

[48] P. Miao, W. Zheng, S. Yang, B. Wu, B. Cheng, J. Tu, H. Ke, W. Yang, J. Wang, J. Cui, and Q. Lin, Wide-range and self-locking atomic magnetometer based on free spin precession, J. Opt. Soc. Am. B **36**, 819 (2019).

[49] L. Zhang, Y. Yang, N. Zhao, J. He, and J. Wang, A multipass optically pumped rubidium atomic magnetometer with free induction decay, Sensors **22**, 7598 (2022).

[50] N. Wilson, C. Perrella, R. Anderson, A. Luiten, and P. Light, Wide-bandwidth atomic magnetometry via instantaneous-phase retrieval, Phys. Rev. Res. **2**, 013213 (2020).

[51] J. C. Visschers, E. Wilson, T. Conneely, A. Mudrov, and L. Bougas, Rapid parameter determination of discrete damped sinusoidal oscillations, Opt. Express **29**, 6863 (2021).

[52] P. Bloomfield, in *Fourier Analysis of Time Series: An Introduction* (John Wiley & Sons, New York, 2000).

[53] M. K. Plante, D. L. MacFarlane, D. D. McGregor, R. E. Slocum, W. M. Sampson, and A. W. Brown, Generalized theory of double-resonance optical pumping of ^{4}He, Phys. Rev. A **82**, 013837 (2010).

[54] J. Rutkowski, *Study and realization of a miniature isotropic helium magnetometer*, Ph.D. thesis, University of Franche-Comté, 2014.

[55] V. Gerginov, F. C. S. da Silva, and D. Howe, Prospects for magnetic field communications and location using quantum sensors, Rev. Sci. Instrum. **88**, 125005 (2017).

[56] A. Serafin, M. Fadel, P. Treutlein, and A. Sinatra, Nuclear spin squeezing in helium-3 by continuous quantum nondemolition measurement, Phys. Rev. Lett. **127**, 013601 (2021).